Evolution of static charge density wave order, amplitude mode dynamics, and suppression of Kohn anomalies at the hysteretic transition in math xmlns="http://www.w3.org/1998/Math/MathML">msub>mrow>mi>EuTe/mi>/mrow>mn>4/mn>/msub>/math>

Ranjana Rathore, Abhishek Pathak, Mayanak K. Gupta, Ranjan Mittal, Ruta Kulkarni, A. Thamizhavel, Himanshu Singhal, Ayman H. Said, and Dipanshu Bansal

Phys. Rev. B **107**, 024101 — Published 4 January 2023

DOI: 10.1103/PhysRevB.107.024101

Evolution of static charge-density-wave order, amplitude mode dynamics, and suppression of Kohn anomalies on hysteretic transition in $EuTe_4$

Ranjana Rathore[1,2], Abhishek Pathak[3], Mayanak K Gupta[2,4], Ranjan Mittal[2,4], Ruta Kulkarni[5], A. Thamizhavel[5], Himanshu Singhal[1,2], Ayman H Said[6], and Dipanshu Bansal[3,7]

[1] *Laser Plasma Division, Raja Ramanna Centre for Advanced Technology, Indore MP 452013, India*

[2] *Homi Bhabha National Institute, Anushaktinagar, Mumbai MH 400094, India*

[3] *Department of Mechanical Engineering, Indian Institute of Technology Bombay, Mumbai, MH 400076, India*

[4] *Solid State Physics Division, Bhabha Atomic Research Centre, Mumbai, MH 400085, India*

[5] *Department of Condensed Matter Physics & Materials Science, Tata Institute of Fundamental Research, Mumbai, MH 400005, India*

[6] *Advanced Photon Source, Argonne National Laboratory, 9700 South Cass Avenue, Lemont, IL 60439, USA and*

[7] *Center for Research in Nano Technology and Science, Indian Institute of Technology Bombay, Mumbai, MH 400076, India*

(Dated: December 22, 2022)

Abstract

Charge-density-wave (CDW) induces periodic spatial modulation of the charge density that is commensurate or incommensurate with the host lattice periodicity, and leads to partial or complete electronic bandgap opening at the Fermi level (E_F). The recent finding of unconventional hysteresis within the CDW phase of $EuTe_4$, not observable in other rare-earth tellurides $R\mathrm{Te}_n$ (n = 2, 3), has highlighted the role of the relative phase of CDW distortion in weakly coupled Te layers. However, detailed structural and dynamical characterization of CDW distortion on the hysteretic transition is lacking. Here we report on the static CDW order, dynamics of the amplitude mode, and their evolution on the hysteretic transition using meV resolution elastic and inelastic x-ray scattering. We discover previously unidentified multiple commensurate and incommensurate CDW wavevectors $\mathbf{q}_{\mathrm{CDW}}$ along all three crystallographic axes. Importantly, we find that the previously reported b-axis CDW peak is coupled with the interlayer CDW phase and consequently co-occurs with the doubling of the unit cell along the c-axis. We confirm the presence of the competing a-axis CDW order but found it to be four orders of magnitude weaker than the b-axis CDW. Furthermore, we observe multiple Kohn anomalies at $\mathbf{q}_{\mathrm{CDW}}$ driven by Fermi surface nesting and hidden nesting, confirming earlier reports based on electronic and lattice susceptibility simulations. The amplitude mode and Kohn anomalies are found to suppress on unconventional hysteretic transition, suggesting the presence of non-degenerate metastable states, which we identify from the x-ray scattering measurements and simulations.

CDW is ubiquitous in rare-earth tellurides family, $R\mathrm{Te}_n$ ($n = 2$, 3, and 4), with unstable square-net Te planes undergoing planar distortion forming Te trimers below the transition temperature T_{CDW} (see Fig. 1).[1–16] Despite the commonality of the planar distortion for the entire family,[17] critical distinctions exist for different n, thus leading to vastly different properties. First distinction is in the crystal structure, where for $n = 2$, one square-net Te plane (Te monolayer) is sandwiched between two corrugated (RTe) planes, i.e., $(R\mathrm{Te})_2{-}\underline{\mathrm{Te}}{-}\cdots$,[2,3] whereas for $n = 3$, two adjacent Te planes (Te bilayer) alternate with two (RTe) planes, i.e., $(R\mathrm{Te})_2{-}\overline{\overline{\mathrm{Te}}}{-}\overline{\overline{\mathrm{Te}}}{-}\cdots$[4,7] (see Supplementary Material (SM) Fig. S1,[18] see, also, references 19–27 therein). Here underline and overline imply Te atoms in monolayer and bilayer, respectively. In contrast to both the $n = 2$ and 3 series, in the recently synthesized $n = 4$ compound EuTe_4, the Te monolayer and bilayer separated by (EuTe) plane co-exists, i.e., $(\mathrm{EuTe}){-}\underline{\mathrm{Te}}{-}(\mathrm{EuTe}){-}\overline{\overline{\mathrm{Te}}}{-}\overline{\overline{\mathrm{Te}}}{-}\cdots$ (see Fig. 1).[14] Because of the co-existence, the planar distortion of the Te monolayer and two Te layers in a bilayer can have different phases, ϕ_1, ϕ_2, and ϕ_3, thus introducing an additional degree of freedom $\phi = \phi_1 - \phi'$ in EuTe_4 ($\phi' = \phi_2 - \phi_3$). The metastable degenerate three-dimensional domain structures for $\phi = 0$ and π (keeping $\phi' = \pi$) are proposed to be separated by a large energy barrier of the order of eV and the root cause of unconventional hysteresis loop spanning $\sim$400 K in EuTe_4.[15] Here the transition is referred to as unconventional hysteretic as the hysteresis loop occurs well below T_{CDW} owing to CDW distortion phase change with no change in CDW wavevector $\mathbf{q}_{\mathrm{CDW}}$.[15]

The second distinction is in the valency of rare-earth ions. In the $n = 2$ and 3 series, R is trivalent, which fills the Te p orbitals within the RTe plane and donates an extra electron to partially fill Te p orbitals in monolayer or bilayer planes. On the other hand, due to the divalency of R in $n = 4$, no electron transfer occurs between the RTe plane and Te mono- or bilayers.[15] Thirdly, the Fermi surface is fully gapped for $n = 4$,[15,28] but remnant metallic pockets are present for $n = 3$.[5,6]. The charge neutrality of Te planes and lack of available free carriers possibly set the energy scale of Te monolayer and bilayer coupling, thus controlling the ϕ and the domain structure.[15]

Another contentious point in the literature is the origin of CDW.[29–31] For example, in multiple $R\mathrm{Te}_3$ compounds, based on angle-resolved photoemission spectroscopy (ARPES) measurements, CDW is found to originate from (imperfect) Fermi surface nesting (FSN).[6] On the other hand, inelastic x-ray scattering (IXS) measurements of TbTe_3 and DyTe_3[9,10] showed *wavevector-dependent* electron-phonon interaction (EPI) induced softening of a phonon branch at $\mathbf{q}_{\mathrm{CDW}}$, a markedly different mechanism than FSN. In comparison, for $R\mathrm{Te}_2$, ARPES and diffraction measurements have pointed towards FSN driven CDW.[2,3] Similar to $R\mathrm{Te}_2$ and a few $R\mathrm{Te}_3$, using explicit simulations of electron and lattice susceptibility of EuTe_4, imperfect FSN combined with hidden nesting owing to linearly dispersing bands near the Fermi energy (E_{F}) is found to be the origin of CDW.[14,16] ARPES measurements recently confirmed the presence of imperfect FSN.[28] But to unequivocally confirm the FSN and hidden nesting driven CDW, we must observe multiple Kohn anomalies at $\mathbf{q}_{\mathrm{CDW}}$[16,29,32] instead of a single phonon branch.[9,10,33] CDW driven by other mechanisms such as strong electron correlations[30,34,35] and large electronic density-of-states (EDOS) at E_{F} in high-symmetry structures[36,37] can be safely excluded as both strong correlations and large EDOS at E_{F} are absent.[16]

Besides the observation of Kohn anomalies, whether they are induced by imperfect FSN and hidden nesting or wavevector-dependent EPI, it is critical to understand the evolution of Kohn anomalies and amplitude mode on unconventional hysteresis. The amplitude mode corresponds to oscillations of the CDW order parameter. Here the observed unconventional hysteresis is to be differentiated with hysteresis due to incommensurate to commensurate CDW or metal-to-CDW transition as discussed in Ref. 15. Hence, a priori, we have little knowledge of whether the Kohn anomalies and amplitude mode will remain the same, suppress, or strengthen in the metastable states. Such evolution can further show how the static CDW order influences lattice dynamics. Moreover, as reported earlier,[16] both a and b axes CDWs compete with each other, but due to the larger strength of the electronic instability, long-range CDW order is established along the b axis. However in literature, the long-range ordering of the competing axes is observed for some of the $R\mathrm{Te}_3$ compounds ($R =$ Dy, Ho, Er, and Tm)[7] on further cooling or on photoexcitation.[12] Hence, the investigation of competing a-axis CDW on hysteresis is necessary to identify (dis)similarities with other rare-earth tellurides.

In this combined experimental and simulation study, we report both the long-range static CDW order and associated Kohn anomalies in EuTe_4 to elucidate the above-raised questions about long-range CDW order, the origin of CDW, the evolution of Kohn anomalies, and competing a-axis CDW on hysteresis. Using single-crystal elastic x-ray scattering (EXS) [to be differentiated from single-crystal x-ray diffraction (XRD)], we identify previously unknown multiple $\mathbf{q}_{\mathrm{CDW}}$ along all three axes. The experimental observation of multiple

Kohn anomalies at $\mathbf{q}_{\mathrm{CDW}}$ using IXS confirms that the b-axis CDW is driven by FSN and hidden nesting, hence confirming the previous simulation proposition. Notably, we find that the Kohn anomalies along the b-axis are suppressed and the intensity of the competing a-axis CDW nearly vanishes on unconventional hysteretic transition (300 K→30 K→50 K→300 K). We further discover the metastable states that possibly control the unconventional hysteretic transition.

CDW transition

$EuTe_4$ crystallizes in the orthorhombic structure ($Pmmn$) in the unmodulated state.[14] Previous studies[14,15] did not measure the T_{CDW} but estimated it to be above the mean-field temperature of 646 K.[15] Using small single-crystal of $EuTe_4$, we measured the heat flow up to 850 K (see SM for details) and found T_{CDW} on heating and cooling cycles to be ∼726 and 652 K, respectively (see Fig. 1d). Below T_{CDW}, $EuTe_4$ undergoes an unconventional hysteresis extending from 50 to 400 K, as evident from XRD, resistivity, and ARPES measurements.[15] We did not observe the onset of unconventional hysteresis in the heat flow measurements near 400 K, either on heating or cooling cycles, possibly due to a small change in the heat capacity. Nevertheless, we measured similar changes as reported in Ref. 15 corresponding to the unconventional hysteresis in the EXS intensity as discussed below.

Evolution of static CDW order

CDW along the b-axis

First, let us distinguish the EXS from XRD measurements. In XRD, the energy bandwidth of the incoming beam and detected beam is large, and the measured intensity includes the integration of the elastic and inelastic signals within the energy bandwidth, which is typically on the order of a few eVs. On the other hand, EXS uses a highly monochromatized beam (ΔE=1 meV), and the detection system includes high-resolution analyzers; the overall energy resolution of the instrument is ∼1.3 to 1.5 meV. Here the detected intensity is the elastic scattering within the instrument energy resolution. Hence, EXS, as opposed to the XRD signal, allows us to distinguish between the intensity arising from long-range static ordering and low-energy phonons. This distinction allowed us to delineate long-range ordering along the competing a-axis, as discussed later in the text.

Figure 2a shows the EXS scan along $[4, K, 0]$ to identify the CDW peaks corresponding to the trimer formation in Te mono- and bilayer below T_{CDW}. All $[H, K, L]$ notations in the text correspond to the unmodulated state structure. Consistent with previous single-crystal XRD measurements, we observe a CDW peak at $\mathbf{q}^K_{\mathrm{CDW1}} = 0.643(1)$ r.l.u. at 300 K. In addition, we observe higher-order (2^{nd} and 4^{th} order) CDW peaks in the same scan as marked by arrows in the figure. The same plot is shown on the logarithmic scale in panel (b), where we further mark the higher-order peaks up to 10^{th} order. Higher-order peak positions allow us precisely determine the $\mathbf{q}^K_{\mathrm{CDW1}}$ and affirm its incommensurate nature. In panel (a), we also show the peak intensity evolution as we scan through the unconventional hysteresis loop by following the 300 K→30 K→50 K→300 K thermal cycle. Consistent with previous single-crystal XRD measurements,[15] the peak intensity at $\mathbf{q}^K_{\mathrm{CDW1}}$ increases nearly 1.7 times at 300 K on thermal cycling. On comparison, the intensity and mosaic of the nearby (4,0,0) Bragg peak remained the same on thermal cycling (see SM Fig. S3a). The observed increase of the peak intensity at $\mathbf{q}^K_{\mathrm{CDW1}}$ could be due to an increase in correlation length ξ, CDW distortion amplitude Q_{CDW} of mono- and bilayers (i.e., Te-Te distance in the trimers), or relative phase of distortions (ϕ and ϕ'). The ξ can directly be calculated from the spatial spread of the CDW peak in the reciprocal space. However, the width of $\mathbf{q}^K_{\mathrm{CDW1}}$ is limited by our instrument resolution and step size, which put a lower limit of ∼400 Å on ξ. We will discuss the Q_{CDW} and relative phase, and their implications on the intensity later in the text.

Next, we focus on the observation of two more CDW peaks along K, which so far have remained elusive. Figure 2c shows the EXS scan along $[0, K, -0.5]$. We observe a central peak at $(0, 2, -0.5)$ flanked by multiple satellite peaks, as marked by the arrows. Since the intensity of satellite peaks appears at a periodic K interval and decreases away from the central peak, they are higher-order CDW peaks. Hence, we can assign the $\mathbf{q}^K_{\mathrm{CDW2}}$ to be 0.035(5) r.l.u. The appearance of the CDW peaks at $\mathbf{q}^K_{\mathrm{CDW2}}$ for $L = -0.5$ further indicates that $\mathbf{q}^K_{\mathrm{CDW2}}$ co-occurs with the doubling of the unit cell along the c-axis. We will discuss the doubling along the c-axis later in the text along with the c-axis CDW. As shown in Fig. 2d, the EXS scan along $[0, K, -1]$ revealed an additional CDW along K. We observe a Bragg peak at $(0, 2, -1)$ and multiple satellite peaks, as marked by the arrows. Unlike satellite peaks of $(0, 2, -0.5)$, the intensity does not decrease monotonically away from (0,2,-

1), which suggests them to be higher-order CDW peaks. Based on their periodic appearance and intensity variation away from $(0, 2, -1)$, we identify $\mathbf{q}^K_{\text{CDW3}}$ to be 0.965(5) r.l.u. Here the second-order CDW peaks, i.e., $(0, 2\mathbf{q}^K_{\text{CDW3}}, -1)$ and $(0, 4 - 2\mathbf{q}^K_{\text{CDW3}}, -1)$, are stronger than the first-order peaks, i.e., $(0, 1 + \mathbf{q}^K_{\text{CDW3}}, -1)$ and $(0, 3 - \mathbf{q}^K_{\text{CDW3}}, -1)$, as they are satellites of relatively intense Bragg peaks $[(0, 0, -1)$ and $(0, 4, -1)]$ compared to the first-order peaks that are satellites of weak Bragg peaks $[(0, 1, -1)$ and $(0, 3, -1)]$. We note that $\mathbf{q}^K_{\text{CDW2}}$ and $\mathbf{q}^K_{\text{CDW3}}$ may appear to be the same or related as they can be expressed as $\mathbf{q}^K_{\text{CDW2}} = 1 - \mathbf{q}^K_{\text{CDW3}}$ within the error bars; however, we could not find evidence from the measured data for them to be related; hence we denote them independently. We emphasize that the periodic appearance of CDW peaks on either side of a central peak in multiple Brillouin zones rules out two or more flakes or multiple scattering contributing to the measured intensity.

CDW along the c-axis

Figure 3a shows the EXS scan along $[0, 4, L]$. We observe a CDW peak at $\mathbf{q}^L_{\text{CDW1}} =$ 0.50(1) r.l.u. at 300 K, as marked by the red arrow. Surprisingly, on thermal cycling to 50 K. (i.e., 300 K→30 K→50 K), the peak at $\mathbf{q}^L_{\text{CDW1}}$ loses intensity and becomes broad. On further heating to 300 K, it regains its intensity but is much narrower. We quantify ξ by fitting the peak with the Gaussian function.[38] Here $\xi = 1/\pi/\text{FWHM}$, and FWHM is the full-width-half-maximum of the Gaussian fitting. The ξ is found to initially decrease from 72 Å at 300 K to 44 Å at 50 K, and then increase to 106 Å on heating back to 300 K.

The peak at $\mathbf{q}^L_{\text{CDW1}}$ corresponds to a doubling of the unit cell along the c-axis. This doubling can be due to the out-of-phase displacement of Te mono- and/or bilayers in the adjacent unit cell, i.e., $(\text{EuTe}){-}\underline{\text{Te}\uparrow}{-}(\text{EuTe}){-}\overline{\overline{\text{Te}\uparrow}}{-}\overline{\overline{\text{Te}\downarrow}}{-}{::}(\text{EuTe}){-}\underline{\text{Te}\downarrow}{-}(\text{EuTe}){-}\overline{\overline{\text{Te}\uparrow}}{-}\overline{\overline{\text{Te}\downarrow}}{-}\cdots$, or equivalently phase shift β along the b-axis in Te mono- and/or bilayer in the adjacent unit cell (see Fig. 4a). Here underline and overline implies Te atoms in monolayer and bilayer, $\uparrow$ and $\downarrow$ indicate the phase of the distortion, and $::$ separate the two adjacent unit cells. For example, the above configuration indicates that the unit cell is doubled along the c-axis due to out-of-phase distortion of the Te monolayer in the adjacent unit cells. From measured values of ξ, it is apparent that the extent of correlation of such displacements decreases on cooling, leading to a decrease in the measured intensity at 50 K. Similarly, the rise in intensity on heating back to 300 K is due to the increase in ξ.

Next, we focus on three more CDW peaks along L. Figure 3b shows the EXS scan along $[0, 3, L]$ spanning multiple Brillouin zones. In all Brillouin zones, we observe $\mathbf{q}^{L}_{\mathrm{CDW1}}$ (marked by the red arrows), and also a repeated pattern of intensity emanating corresponding to $\mathbf{q}^{L}_{\mathrm{CDW2}} = 0.071(5)$ r.l.u., as marked by the black arrows. Similarly, as shown in Fig. 3(c,d), we observe two more CDWs at $\mathbf{q}^{L}_{\mathrm{CDW3}} = 0.045(5)$ and $\mathbf{q}^{L}_{\mathrm{CDW4}} = 0.10(1)$ along $[0, 2, L]$ and $[0, 4, L]$, respectively (marked by the black arrows). In all of these scans, the CDW peaks corresponding to $\mathbf{q}^{L}_{\mathrm{CDW1}}$ are visible. None of these CDW peaks were reported in the earlier studies.[14,15]

In addition to the above CDW peaks, we also observe peaks corresponding to the combination of b- and c-axes CDWs. Figure 4b shows one such EXS scan along $[0, K, -3.5]$. The peak at $K = 2.714$ r.l.u. corresponds to a combination of $\mathbf{q}^{K}_{\mathrm{CDW1}}$ and $\mathbf{q}^{L}_{\mathrm{CDW1}}$. We identify the peak to be a satellite of the $(0, 4, -4)$ Bragg peak such that the peak position in terms of $\mathbf{q}^{K}_{\mathrm{CDW1}}$ and $\mathbf{q}^{L}_{\mathrm{CDW1}}$ can be written as – $(0{,}4{-}2\mathbf{q}^{K}_{\mathrm{CDW1}}, -4 + \mathbf{q}^{L}_{\mathrm{CDW1}})$. Similarly, we identify the peak at $K = 2.678$ to be a combination of two first order CDW peaks along K (i.e., $\mathbf{q}^{K}_{\mathrm{CDW1}}$ and $\mathbf{q}^{K}_{\mathrm{CDW2}}$) and a first-order peak along L (i.e., $\mathbf{q}^{L}_{\mathrm{CDW1}}$) such that the peak position can be expressed as $(0,\ 2{+}\mathbf{q}^{K}_{\mathrm{CDW1}}{+}\mathbf{q}^{K}_{\mathrm{CDW2}}, -4 + \mathbf{q}^{L}_{\mathrm{CDW1}})$. The remaining satellite peaks are labeled in the figure. The observation of such peaks has critical implications. For example, if we pick the peak at $K = 2.714$, it implies that trimer formation (i.e., $\mathbf{q}^{K}_{\mathrm{CDW1}}$) co-occurs with doubling of the c-axis (i.e., $\mathbf{q}^{L}_{\mathrm{CDW1}}$), and are not independent. Figure 4a shows one representative mix distortion where Te-Te trimers in the bilayer are phase-shifted by β along the b-axis in the adjacent unit cells (see across the black dotted line in the figure). Later in the text, we will discuss more on this from the system energy minimization perspective using simulations.

CDW along the a-axis

Figure 5a shows the EXS scan along $[H, 0, 0]$ to identify if a long-range order is also established along the competing a-axis. We observe a peak at $\mathbf{q}^{H}_{\mathrm{CDW}} = 0.604(5)$ r.l.u., although it is substantially weaker in the intensity ($\sim$60 counts for $\mathbf{q}^{H}_{\mathrm{CDW}}$ as opposed to $\sim 3.5\times10^{5}$ counts $\mathbf{q}^{K}_{\mathrm{CDW1}}$ per 5 seconds) and have much smaller $\xi \sim 50$ Å at 300 K. It implies, besides the shorter correlation length, Q_{CDW} of competing a-axis CDW is significantly smaller than the b-axis. On thermal cycling (300 K→30 K→50 K→300 K), the peak intensity at $\mathbf{q}^{H}_{\mathrm{CDW}}$ drops by a factor of four, essentially indicative of suppression of long-range CDW order along the a-axis. Another interesting observations is the position of $\mathbf{q}^H_{\mathrm{CDW}}$, which is different from $\mathbf{q}^K_{\mathrm{CDW1}}$, in spite of similar lattice parameters ($a = 4.512$ Å and $b = 4.635$ Å). If we compare the experimental values of $\mathbf{q}^K_{\mathrm{CDW1}}$ and $\mathbf{q}^H_{\mathrm{CDW}}$ with the density functional theory simulations in the unmodulated structure of Pathak *et al.*,[16] $\mathbf{q}^K_{\mathrm{CDW1}} = 0.65$ r.l.u. agrees well with the measured value [0.643(1)], but simulated $\mathbf{q}^H_{\mathrm{CDW}} = 0.67$ differs from our measurements, which may suggest renormalization of the electronic bands along H due to the presence of $\mathbf{q}^K_{\mathrm{CDW1}}$. However, due to the unavailability of evidence of band renormalization along H from ARPES measurements,[15,28] we should exercise caution in the interpretation. We note that two peaks at $H = 2.30$ and 2.57 r.l.u. were also observed while scanning along $[H, 0, 0]$ ($2 < H < 3$, see Fig. 5b), but despite measurements in multiple Brillouin zones (no peak was observed while scanning between $3 < H < 4$), we could not find evidence of them to be related to $\mathbf{q}^H_{\mathrm{CDW}}$ via any higher-order CDW peaks. Hence, we could not find their origin and do not label them.

Observation of multiple Kohn anomalies at $\mathbf{q}_{\mathrm{CDW}}$

After establishing the static CDW order along all three axes, we now focus on its phonon dynamics. Recently, using electron and lattice susceptibility calculations in the unmodulated structure, Pathak *et al.* predicted multiple Kohn anomalies at $\mathbf{q}^K_{\mathrm{CDW1}}$ owing to the FSN and hidden nesting.[16] Fundamentally, as described in the seminal paper by W. Kohn,[39] the Kohn anomaly emerges due to sudden change in electron screening across $\mathbf{q}_{\mathrm{CDW}}$, which consequently alters the interatomic forces and lead to strong perturbation of phonons at $\mathbf{q}_{\mathrm{CDW}}$. The perturbation is visible as a dip or a kink in the phonon dispersion. Kohn anomaly induced only by FSN is localized at $\mathbf{q}_{\mathrm{CDW}}$, for example, as observed for $ZrTe_3$ and (3,3) carbon nanotubes.[40,41] However, if electronic bands linearly disperse near E_{F}, then energy states above and below E_{F} also contribute to the electronic instability (i.e., hidden nesting) and consequently to the Kohn anomaly.[16,29,32] The Kohn anomaly here is not localized and follows the distinct power law dependence, as theoretically derived for the linearly dispersing bands in Weyl semimetals and experimentally observed for TaP.[42]

Kohn anomalies in $EuTe_4$ at $\mathbf{q}^K_{\mathrm{CDW1}}$ emerge above T_{CDW} in the unmodulated structure.[16] The condensation of transverse acoustic branch at $\mathbf{q}^K_{\mathrm{CDW1}}$ (shown as negative frequency in

SM Fig. S8a) induces a static CDW order below T_{CDW}. However, the signature of the Kohn anomaly in other phonon branches at $\mathbf{q}^{K}_{\mathrm{CDW1}}$ will be observable below T_{CDW}. On subsequent cooling, acoustic and amplitude modes appear at $\mathbf{q}^{K}_{\mathrm{CDW1}}$, as qualitatively illustrated in SM Fig. S9. The eigenvectors of the amplitude mode correspond to the CDW distortion. Figure 6a shows the measured phonon energies along $[4, K, 0]$ ($0 < K < 1$) using IXS at 300 K at HERIX beamline (see SM for experimental details, and SM Fig. S4 and S5 for raw data). The $[4, K, 0]$ direction selectively probes a-polarized phonons propagating along K, eigenvectors of which overlap with the CDW distortion enabling Te trimer formation.[16] As expected, we observe the amplitude mode at $\sim$4.5 meV (see dispersion at low energies), and a Kohn anomaly in the optic branch near $\sim$11 meV at $\mathbf{q}^{K}_{\mathrm{CDW1}} = 0.643(1)$ r.l.u. (marked by the light green line).

If the electron screening suddenly changes at $\mathbf{q}_{\mathrm{CDW}}$ due to FSN and hidden nesting, not only the phonons enabling the static CDW order (or having the same polarization as CDW distortion), but other phonon branches ($b-$ and c-polarized) at $\mathbf{q}_{\mathrm{CDW}}$ must also harbor Kohn anomalies.[16,29,32] Recently, using electronic and lattice susceptibility simulations and inelastic neutron scattering measurements, multiple phonon Kohn anomalies were observed at $\mathbf{q}_{\mathrm{CDW}}$ in α-U.[32] To confirm multiple Kohn anomalies at $\mathbf{q}^{K}_{\mathrm{CDW1}}$ in $EuTe_4$, we first measured phonon energies along $[0, K, 0]$ ($3 < K < 4$, see Fig. 6b). The $[0, K, 0]$ direction selectively probes b-polarized phonons propagating along K, i.e., longitudinal acoustic and optic phonons. Kohn anomalies at $\mathbf{q}^{K}_{\mathrm{CDW1}}$ are visible from the measured dispersions. Similarly, we also measured phonon energies along $[0, K, 10]$ that selectively probes the c-polarized phonons propagating along K,i.e, transverse acoustic and optic phonons (see SM Fig. S6). Kohn anomaly can be observed in both acoustic and optics branches $\mathbf{q}^{K}_{\mathrm{CDW1}}$. Hence, from the measured data for a-, b-, and c-polarized branches propagating along K, we confirm the presence of multiple Kohn anomalies in $EuTe_4$ at $\mathbf{q}^{K}_{\mathrm{CDW1}}$, as earlier also shown to occur using lattice dynamical susceptibility simulations.[16]

Next, we focus on the Kohn anomalies along the competing H direction. As discussed earlier, the static CDW order distortion along the a-axis is much weaker than the b-axis. Hence, a priori, it is not clear if the Kohn anomaly will be visible along H. However, simulations in the unmodulated structure predict lattice instability at $\mathbf{q}^{H}_{\mathrm{CDW}}$ (see SM Fig. S8c). We measured the phonon energies along $[H, 4, 0]$ direction to selectively probe b-polarized phonons propagating along H, i.e., transverse acoustic and optic phonons. As one can observe from Fig. 7a, the Kohn anomaly is visible in the acoustic branch at $\mathbf{q}^{H}_{\mathrm{CDW}}$. Since the Kohn anomalies along H are also driven by similar FSN and hidden nesting, to confirm multiple Kohn anomalies along H, we measured along $[H, 0, 0]$ direction that selectively probes a-polarized phonons propagating along H, i.e., longitudinal acoustic and optic phonons (see SM Fig. S7). The Kohn anomaly along $[H, 0, 0]$ is evident at $\mathbf{q}^{H}_{\mathrm{CDW}}$.

Lattice dynamics evolution on unconventional hysteretic transition

After mapping the amplitude mode and Kohn anomalies along a- and b-axes, we now investigate their evolution on unconventional hysteretic transition. Figure 6c shows measured phonon energies at 300 K along $[4, K, 0]$ following the 300 K→30 K→300 K thermal cycle (see SM Fig. S5 for raw data). As one can observe, the large dip corresponding to the amplitude mode in panel (a) at $\mathbf{q}^{K}_{\mathrm{CDW1}}$ has suppressed on thermal cycling. The suppression of dip could be due to phonon renormalization from changes in atomic positions (for example, amplitude Q_{CDW} and relative phase of Te mono- and bilayer, i.e., ϕ and ϕ') or trivially related to expected phonon softening/stiffening on first-order CDW phase transition. We note that the CDW transition here is first-order in nature, as evident from different T_{CDW} on heating and cooling (see Fig. 1d). We discuss below both scenarios.

First, we discuss the expected phonon softening/stiffening on first-order CDW phase transition, qualitatively illustrated in SM Fig. S9. As described earlier, the $[4, K, 0]$ direction probes Te-Te trimer distortion that induces the CDW transition along the b-axis. Above T_{CDW}, the phonon energy extracted from IXS scans along $[4, K, 0]$ will have a minima at $\mathbf{q}^{K}_{\mathrm{CDW1}}$. The phonon energy at $\mathbf{q}^{K}_{\mathrm{CDW1}}$ will continue to decrease on cooling from $T > T_{\mathrm{CDW}}$ to T_{CDW} and dropping to zero at T_{CDW}, thus leading to a CDW peak. On cooling below $T^{cooling}_{\mathrm{CDW}}$, acoustic phonons will emerge from the CDW peak along with the amplitude mode. We did observe weak acoustic phonon intensity emanating from $\mathbf{q}^{K}_{\mathrm{CDW1}}$ (see SM Fig. S5). Since the amplitude mode is indicative of oscillations in the CDW order parameter, its energy will continuously increase on cooling below $T^{cooling}_{\mathrm{CDW}}$. This expected trend is observed across phase transitions in several materials.[43] On subsequent heating, the amplitude mode energy will drop to zero at $T^{heating}_{\mathrm{CDW}}$, as shown in SM Fig. S9d.

If the above-described scenario of first-order phase transition is applicable for the suppression of the dip in the amplitude mode observed in Fig. 6c, then the Kohn anomalies in

b- and c-polarized branches (i.e., along $[0, K, 0]$ and $[0, K, 10]$) must not exhibit the suppression. This is because phonon eigenvectors of b- and c-polarizations are different from CDW distortion at $\mathbf{q}^{K}_{\mathrm{CDW1}}$ and they do not condense (i.e., drop to zero energy) at $\mathbf{q}^{K}_{\mathrm{CDW1}}$ below $T^{cooling}_{\mathrm{CDW}}$. Hence, to confirm the origin of suppression, we measured phonon energies along $[0, K, 0]$ on thermal cycling (see Fig. 6d). As one can observe, similar to the suppression in the $[4, K, 0]$ direction, the Kohn anomaly is also suppressed at $\mathbf{q}^{K}_{\mathrm{CDW1}}$. Thus, the above measurements and observations suggest that the renormalization of phonons on thermal cycling must be due to a change in Q_{CDW} or relative phases ϕ and ϕ', and is not a consequence of the first-order CDW phase transition. The role of Q_{CDW} or ϕ and ϕ' is further supported by the measurements of the Kohn anomaly in the competing H axis on thermal cycling (i.e., along the $[H, 4, 0]$ direction). Here the Kohn anomaly essentially remains the same (see Fig. 7b), as mono- and bilayer distortions being perpendicular to the measured polarization do not affect the Kohn anomaly. We note that IXS measurements were attempted at 600 K and above under vacuum; however, the sample was not stable. We observed a continuous decrease of Bragg peak intensity over several hours, suggesting possible evaporation.

Metastable states of unconventional hysteretic transition

Next, we focus on understanding the relative phase difference of mono- and bilayer distortions, ϕ and ϕ'. Note that in the below discussion, we make inferences from the measured data and DFT simulations, and the arguments are by no means conclusive. Firstly, the suppression of the Kohn anomaly on thermal cycling suggests that the two metastable states at 300 K are possibly not degenerate. If two metastable states were degenerate, then we would have observed the similar lattice dynamics; hence ruling out configurations where different values of ϕ and ϕ' lead to degenerate states on thermal cycling, for example, degenerate states $(\mathrm{EuTe}){-}\underline{\mathrm{Te}\uparrow}{-}(\mathrm{EuTe}){-}\overline{\overline{\mathrm{Te}\uparrow}}{-}\overline{\overline{\mathrm{Te}\downarrow}} - {::}(\mathrm{EuTe}){-}\underline{\mathrm{Te}\downarrow}{-}(\mathrm{EuTe}){-}\overline{\overline{\mathrm{Te}\uparrow}}{-}\overline{\overline{\mathrm{Te}\downarrow}}{-}\cdots$ and $(\mathrm{EuTe}){-}\underline{\mathrm{Te}\downarrow}{-}(\mathrm{EuTe}){-}\overline{\overline{\mathrm{Te}\uparrow}}{-}\overline{\overline{\mathrm{Te}\downarrow}} - {::}(\mathrm{EuTe}){-}\underline{\mathrm{Te}\uparrow}{-}(\mathrm{EuTe}){-}\overline{\overline{\mathrm{Te}\uparrow}}{-}\overline{\overline{\mathrm{Te}\downarrow}}{-}\cdots$.

Secondly, the intensity ratios of the (4,0,0) Bragg peak to the $(4,\mathbf{q}^{K}_{\mathrm{CDW1}},0)$ CDW peak at 300 K, measured using EXS measurements are $\sim$29.2 on cooling and $\sim$17.5 on heating cycle. We simulated several configurations of in-phase and out-of-phase distortions as shown in Fig. 8 and obtained the (a) $\sim$36.2, (b) $\sim$537.9, (c) $\sim$122.1, and (d) $\sim$ 78.0 as intensity ratios. If we reduce the distortion amplitude of monolayers to zero in panels (a) and (d), the intensity ratios change to ∼10.7 and ∼245.0, respectively. From the above intensity ratios, we can exclude the configurations of panels (b,c,d) as they substantially exceed the measured ratios. The configuration shown in panel (a) remains one possible arrangement of atoms in the CDW state. The preference for the configuration shown in panel (a) is not surprising, as the similar distortion pattern of the bilayer was also reported for $R\mathrm{Te}_3$ compounds (R = Ce, Pr, Nd).[4] We note that the configuration shown in panels (b) and (d) are equivalent to scenarios I(B) and I(A), respectively, proposed in Ref. 15.

Thirdly, as evident from the appearance of the CDW peak at $(0,4-2\mathbf{q}^{K}_{\mathrm{CDW1}}, -4+\mathbf{q}^{L}_{\mathrm{CDW1}})$ (see Fig. 4b), Te trimers forms simultaneously with doubling of the unit cell along the c-axis. However, it is unclear whether the doubling is due to the out-of-phase displacement of Te mono- and/or bilayers in the adjacent unit cell or equivalently phase shift β along the b-axis in Te mono- and/or bilayer in the adjacent unit cell. The latter configuration is the same as Fig. 8a and was reported to occur on cooling to 80 K by Wu *et al.*[14] To identify the doubling distortion, we simulated both the scenarios and found both are of same energy separated by less than 0.1 meV/atom.

Hence, based on the above experiments and simulations, we propose that the unconventional hysteretic transition is between the following two states: (i) the configuration shown in Fig. 8a on cooling and (ii) the same configuration but with reduced monolayer distortion on heating. In both configurations, Te bilayer trimers in the adjacent unit cells are phase-shifted along the b-axis, as shown in Fig. 4a. As described earlier, the reduction in monolayer distortion leads to the decreased intensity ratio of the Bragg peak to the CDW peak, thus consistent with the measured EXS data. We further calculated the energy barrier of the transition between the two metastable states using nudge elastic band (NEB) simulations and but did not observe any notable barrier (Fig. 8e) that is not compatible with the value obtained from the resistivity relaxation time ($\geqslant$1 eV).[15] If we observe SM Fig. S3, after thermal cycling, the tails of the (4,0,0) and (0,4,0) Bragg peaks are broad due to either strain or multiple domains having different CDW distortion amplitudes leading to a spread in lattice parameters. Consequently, as also suggested by Lv *et al.*,[15] it is likely strain and/or multiple domains control the flipping kinetics and barrier of the unconventional hysteresis.

Summary

In summary, using EXS and IXS measurements combined with DFT simulations, we tracked the evolution of static CDW order on unconventional hysteretic transition in $EuTe_4$. Multiple CDW ordering wavevectors along all three crystallographic axes are identified by extensive mapping in multiple Brillouin zones. We found a weak CDW order in the competing a-axis, which further weakens (nearly disappears) on thermal cycling. Moreover, we observed multiple Kohn anomalies at $\mathbf{q}^{K}_{\mathrm{CDW1}}$, thus confirming that FSN and hidden nesting induce the long-range CDW order and Kohn anomalies. The amplitude mode and Kohn anomalies are suppressed on thermal cycling, suggesting the presence of two metastable non-degenerate states. We further identify the two metastable states driving the unconventional hysteresis; however, further experimental evidence is necessary to confirm them. Our study highlights the necessity of EXS and IXS to measure several orders of magnitude weak static CDW order (for example, $I_{\mathbf{q}^{H}_{\mathrm{CDW}}}/I_{400} \sim 10^{6}$), higher-order CDW peaks for precise determination of $\mathbf{q}_{\mathrm{CDW}}$, distinguish static CDW order from low-energy phonon contribution at $\mathbf{q}_{\mathrm{CDW}}$, identify Kohn anomalies in multiple branches, and unambiguously determine the origin of CDW.

D.B. thanks the financial support from BRNS – DAE under the project no.: 58/14/30/2019-BRNS/11117, and MoE/STARS under the project no.: MoE/STARS-1/345. The simulations were performed at the SPACETIME-II super-computing facility at IITB and ANUPAM super-computing facility at BARC. This research used resources of the Advanced Photon Source, a US Department of Energy (DOE) Office of Science User Facility operated for the DOE Office of Science by Argonne National Laboratory under contract no. DE-AC02-06CH11357.

[1] K. Shin, V. Brouet, N. Ru, Z. Shen, and I. Fisher, Physical Review B **72**, 085132 (2005).

[2] D. Garcia, G.-H. Gweon, S. Zhou, J. Graf, C. Jozwiak, M. Jung, Y. Kwon, and A. Lanzara, Physical Review Letters **98**, 166403 (2007).

[3] E. Lee, D. Kim, J. Denlinger, J. Kim, K. Kim, B. Min, B. Min, Y. Kwon, and J.-S. Kang, Physical Review B **91**, 125137 (2015).

[4] C. Malliakas, S. J. Billinge, H. J. Kim, and M. G. Kanatzidis, Journal of the American Chemical Society **127**, 6510 (2005).

[5] V. Brouet, W. Yang, X. Zhou, Z. Hussain, N. Ru, K. Shin, I. Fisher, and Z. Shen, Physical Review Letters **93**, 126405 (2004).

[6] V. Brouet, W. Yang, X. Zhou, Z. Hussain, R. Moore, R. He, D. Lu, Z. Shen, J. Laverock, S. Dugdale, N. Ru, and I. Fisher, Physical Review B **77**, 235104 (2008).

[7] N. Ru, C. Condron, G. Margulis, K. Shin, J. Laverock, S. Dugdale, M. Toney, and I. Fisher, Physical Review B **77**, 035114 (2008).

[8] G.-H. Gweon, J. Denlinger, J. Clack, J. Allen, C. Olson, E. DiMasi, M. Aronson, B. Foran, and S. Lee, Physical Review Letters **81**, 886 (1998).

[9] M. Maschek, S. Rosenkranz, R. Heid, A. Said, P. Giraldo-Gallo, I. Fisher, and F. Weber, Physical Review B **91**, 235146 (2015).

[10] M. Maschek, D. Zocco, S. Rosenkranz, R. Heid, A. Said, A. Alatas, P. Walmsley, I. Fisher, and F. Weber, Physical Review B **98**, 094304 (2018).

[11] A. Zong, A. Kogar, Y.-Q. Bie, T. Rohwer, C. Lee, E. Baldini, E. Ergeçen, M. B. Yilmaz, B. Freelon, E. J. Sie, *et al.*, Nature Physics **15**, 27 (2019).

[12] A. Kogar, A. Zong, P. E. Dolgirev, X. Shen, J. Straquadine, Y.-Q. Bie, X. Wang, T. Rohwer, I.-C. Tung, Y. Yang, R. Li, J. Yang, S. Weathersby, S. Park, M. E. Kozina, E. J. Sie, H. Wen, P. Jarillo-Herrero, I. R. Fisher, X. Wang, and N. Gedik, Nature Physics **16**, 159 (2020).

[13] S. Seong, E. Lee, Y. S. Kwon, B. I. Min, J. D. Denlinger, B.-G. Park, and J. Kang, Electronic Structure **3**, 024003 (2021).

[14] D. Wu, Q. Liu, S. Chen, G. Zhong, J. Su, L. Shi, L. Tong, G. Xu, P. Gao, and N. Wang, Physical Review Materials **3**, 024002 (2019).

[15] B. Lv, A. Zong, D. Wu, A. Rozhkov, B. V. Fine, S.-D. Chen, M. Hashimoto, D.-H. Lu, M. Li,

Y.-B. Huang, *et al.*, Physical Review Letters **128**, 036401 (2022).

[16] A. Pathak, M. K. Gupta, R. Mittal, and D. Bansal, Physical Review B **105**, 035120 (2022).

[17] W. Tremel and R. Hoffmann, Journal of the American Chemical Society **109**, 124 (1987).

[18] See Supplemental Material [url] for Methods and Supplementary Figures S1-S9, which includes Refs. [19-27].

[19] T. Toellner, A. Alatas, and A. Said, Journal of Synchrotron Radiation **18**, 605 (2011).

[20] A. Said, H. Sinn, and R. Divan, Journal of Synchrotron Radiation **18**, 492 (2011).

[21] S. Lovesey, *Theory of neutron scattering from condensed matter* (Clarendon Press, Oxford, 1984).

[22] G. Kresse and J. Hafner, Physical Review B **47**, 558 (1993).

[23] G. Kresse and J. Furthmüller, Physical Review B **54**, 11169 (1996).

[24] G. Kresse and J. Furthmüller, Computational Materials Science **6**, 15 (1996).

[25] G. I. Csonka, J. P. Perdew, A. Ruzsinszky, P. H. Philipsen, S. Lebègue, J. Paier, O. A. Vydrov, and J. G. Ángyán, Physical Review B **79**, 155107 (2009).

[26] S. Dudarev, G. Botton, S. Savrasov, C. Humphreys, and A. Sutton, Physical Review B **57**, 1505 (1998).

[27] A. Togo and I. Tanaka, Scr. Mater. **108**, 1 (2015).

[28] C. Zhang, Q.-Y. Wu, Y.-H. Yuan, W. Xia, H. Liu, Z.-T. Liu, H.-Y. Zhang, J.-J. Song, Y.-Z. Zhao, F.-Y. Wu, *et al.*, arXiv preprint arXiv:2203.09206 (2022).

[29] M. Johannes and I. Mazin, Physical Review B **77**, 165135 (2008).

[30] X. Zhu, Y. Cao, J. Zhang, E. Plummer, and J. Guo, Proceedings of the National Academy of Sciences **112**, 2367 (2015).

[31] X. Zhu, J. Guo, J. Zhang, and E. Plummer, Advances in Physics: X **2**, 622 (2017).

[32] A. P. Roy, N. Bajaj, R. Mittal, P. D. Babu, and D. Bansal, Physical Review Letters **126**, 096401 (2021).

[33] F. Weber, S. Rosenkranz, J.-P. Castellan, R. Osborn, R. Hott, R. Heid, K.-P. Bohnen, T. Egami, A. Said, and D. Reznik, Physical Review Letters **107**, 107403 (2011).

[34] C.-W. Chen, J. Choe, and E. Morosan, Reports on Progress in Physics **79**, 084505 (2016).

[35] S. Gerber, H. Jang, H. Nojiri, S. Matsuzawa, H. Yasumura, D. Bonn, R. Liang, W. Hardy, Z. Islam, A. Mehta, *et al.*, Science **350**, 949 (2015).

[36] A. Boring and J. Smith, Los Alamos Science **26**, 90 (2000).

[37] P. Söderlind, A. Landa, and B. Sadigh, Advances in Physics **68**, 1 (2019).

[38] W. Tabis, B. Yu, I. Bialo, M. Bluschke, T. Kolodziej, A. Kozlowski, E. Blackburn, K. Sen, E. M. Forgan, M. v. Zimmermann, *et al.*, Physical Review B **96**, 134510 (2017).

[39] W. Kohn, Physical Review Letters **2**, 393 (1959).

[40] M. Hoesch, A. Bosak, D. Chernyshov, H. Berger, and M. Krisch, Physical Review Letters **102**, 086402 (2009).

[41] K.-P. Bohnen, R. Heid, H. Liu, and C. Chan, Physical Review Letters **93**, 245501 (2004).

[42] T. Nguyen, F. Han, N. Andrejevic, R. Pablo-Pedro, A. Apte, Y. Tsurimaki, Z. Ding, K. Zhang, A. Alatas, E. E. Alp, *et al.*, Physical Review Letters **124**, 236401 (2020).

[43] M. Dove, *Introduction to Lattice Dynamics* (Cambridge University Press, Cambridge, 1993).

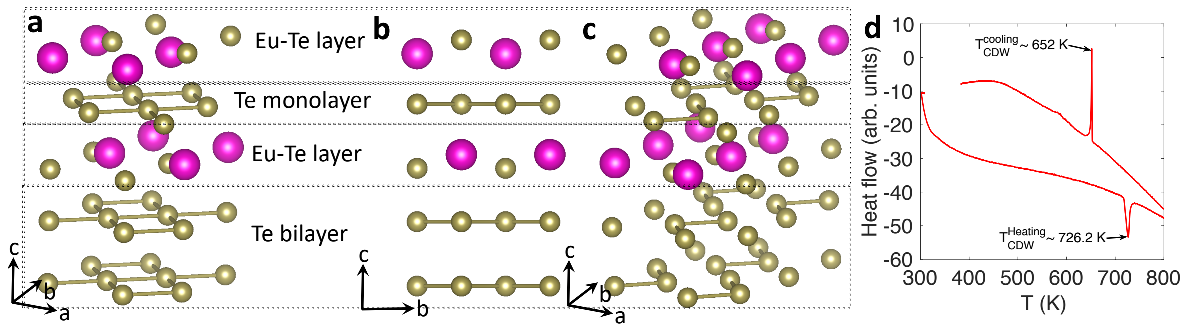

FIG. 1. (a) Unmodulated crystal structure of $EuTe_4$ with Te-Te bonds in Te monolayer and bilayer forming a nearly square pattern. (b) Same as panel (a) but in the b-c plane. (c) Te-Te trimer formation in the monolayer and bilayer in the CDW state. (d) Heat flow in a single-crystal of $EuTe_4$ of mass$\sim$5 mg measured using differential scanning calorimetery under Argon purging. Arrows mark the transitions on heating and cooling.

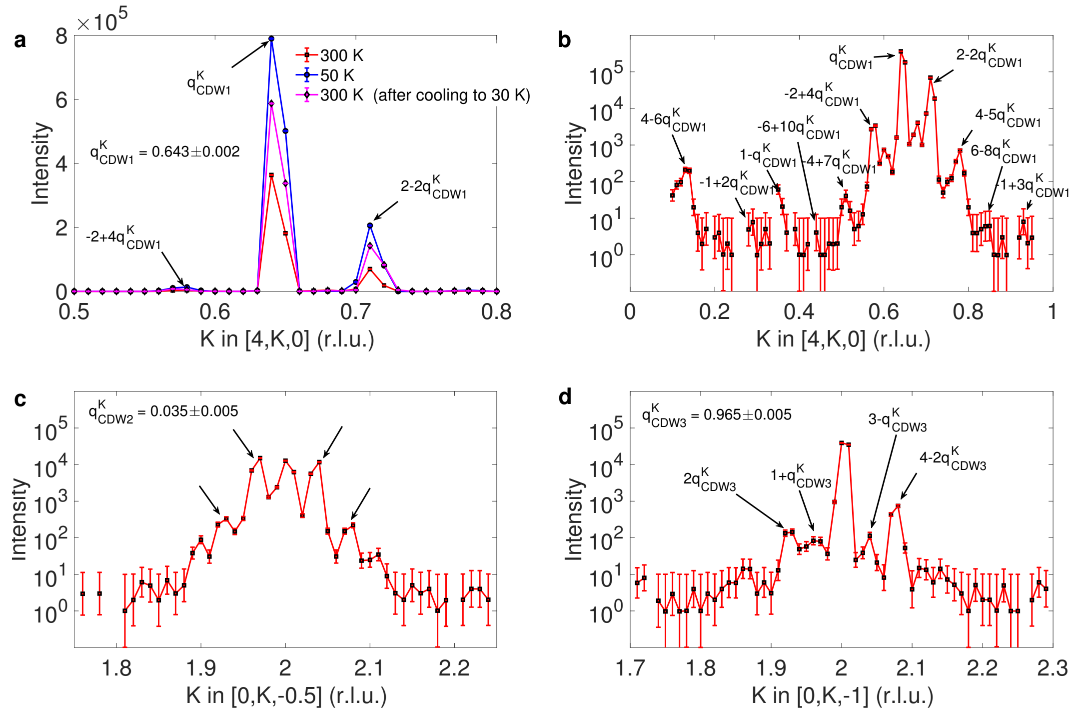

FIG. 2. (a) EXS mapping of CDW state along $[4, K, 0]$ at 300 K, on cooling to 50 K, and after re-heating back to 300 K (thermal cycling 300 K $\rightarrow$ 30 K $\rightarrow$ 50 K $\rightarrow$ 300 K), showing CDW peak corresponding to $\mathbf{q}^K_{\mathrm{CDW1}} = 0.643(1)$ r.l.u. Two higher-order CDW peaks at $K = 0.714$ and 0.572 (2^{nd} and 4^{th} order) corresponding to same $\mathbf{q}^K_{\mathrm{CDW1}}$ are also marked by arrows. Intensity represents the number of EXS photon counts per 5 seconds. Errors bars are from counting statistics ($\sqrt{N}$). (b) Same as panel (a), but counts shown on a logarithmic scale to highlight CDW peaks up to 10^{th} order. (c,d) CDW state along $[0, K, -0.5]$ and $[0, K, -1]$ showing long-range order corresponding to $\mathbf{q}^K_{\mathrm{CDW2}} = 0.035(5)$ and $\mathbf{q}^K_{\mathrm{CDW3}} = 0.965(5)$ r.l.u. Note that the non-labelled peak appearing between $\mathbf{q}^K_{\mathrm{CDW1}}$ and $-2 + 4\mathbf{q}^K_{\mathrm{CDW1}}$ in panel (b) is from CDW distortion $\mathbf{q}^K_{\mathrm{CDW1}} - \mathbf{q}^K_{\mathrm{CDW2}}$. Similarly, the peak between $\mathbf{q}^K_{\mathrm{CDW1}}$ and $2 - 2\mathbf{q}^K_{\mathrm{CDW1}}$ is from $\mathbf{q}^K_{\mathrm{CDW1}} + \mathbf{q}^K_{\mathrm{CDW2}}$.

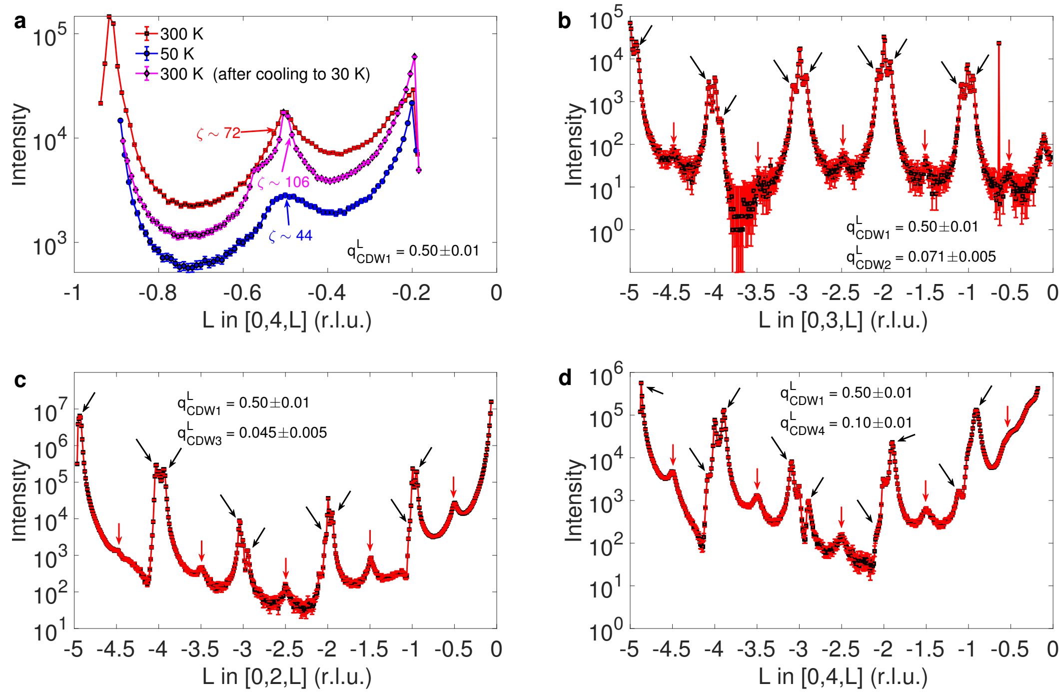

FIG. 3. (a) EXS mapping of CDW state along $[0, 4, L]$ at 300 K, on cooling to 50 K, and after re-heating back to 300 K (thermal cycling 300 K → 30 K → 50 K → 300 K), showing CDW peaks corresponding to $\mathbf{q}^{L}_{\mathrm{CDW1}} = 0.50(1)$ r.l.u. Arrows mark the correlation length ξ at different T. Intensity represents the number of EXS photon counts per 5 seconds. Errors bars are from counting statistics ($\sqrt{N}$). (b,c,d) CDW state along $[0, 3, L]$, $[0, 2, L]$, and $[0, 4, L]$ showing long-range order corresponding to $\mathbf{q}^{L}_{\mathrm{CDW2}} = 0.071(5)$, $\mathbf{q}^{L}_{\mathrm{CDW3}} = 0.045(5)$, and $\mathbf{q}^{K}_{\mathrm{CDW4}} = 0.10(1)$ r.l.u. in multiple Brillouin zones at 300 K. $\mathbf{q}^{L}_{\mathrm{CDW1}}$ is marked by red arrows in panels (b-d), while black arrows in respective panels mark other CDW peaks.

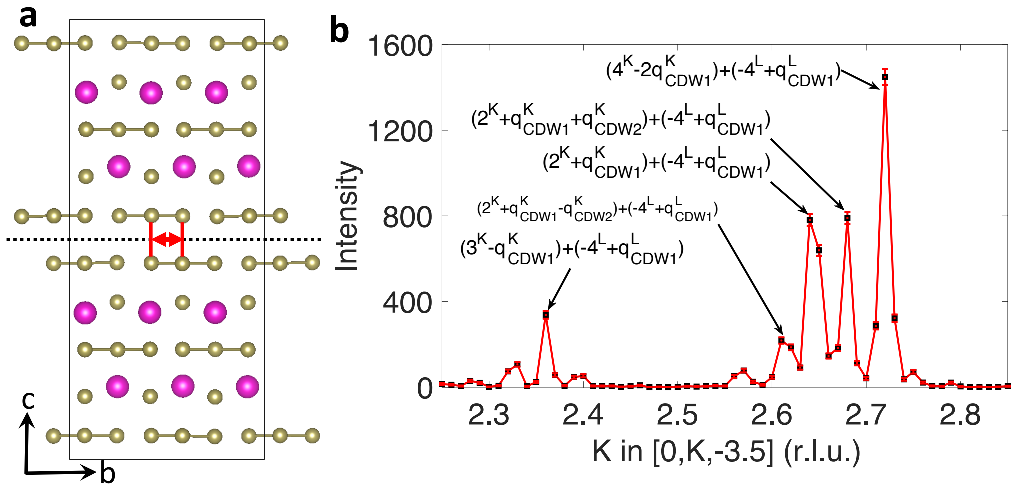

FIG. 4. (a) Phase-shift β of Te trimers in the bilayer along the b-axis in the adjacent unit cells leading to doubling of the unit cell along the c-axis. The red double-headed arrow shows the b-axis phase shift across the black dotted line. In the upper unit cell, ϕ is 0 and ϕ' is π. (b) EXS mapping along $[0, K, -3.5]$ at 300 K showing CDW peaks corresponding to the combined CDW distortion along the b-axis ($\mathbf{q}^K_{\mathrm{CDW1}}$ and $\mathbf{q}^K_{\mathrm{CDW2}}$) and doubling of unit cell along the c-axis ($\mathbf{q}^L_{\mathrm{CDW1}}$). Superscripts on top of numerals (either K or L) indicate the axes. Intensity represents the number of EXS photon counts per 5 seconds. Errors bars are from counting statistics ($\sqrt{N}$). The non-labelled peaks in panel (b) at $K = 2.573$, 2.322, and 2.392 can be expressed as (0, $2+\mathbf{q}^K_{\mathrm{CDW1}}$-$2\mathbf{q}^K_{\mathrm{CDW2}}$, $-4+\mathbf{q}^L_{\mathrm{CDW1}}$), (0, $3-\mathbf{q}^K_{\mathrm{CDW1}}-\mathbf{q}^K_{\mathrm{CDW2}}$, $-4+\mathbf{q}^L_{\mathrm{CDW1}}$), and (0, $3-\mathbf{q}^K_{\mathrm{CDW1}}+\mathbf{q}^K_{\mathrm{CDW2}}$, $-4+\mathbf{q}^L_{\mathrm{CDW1}}$), respectively.

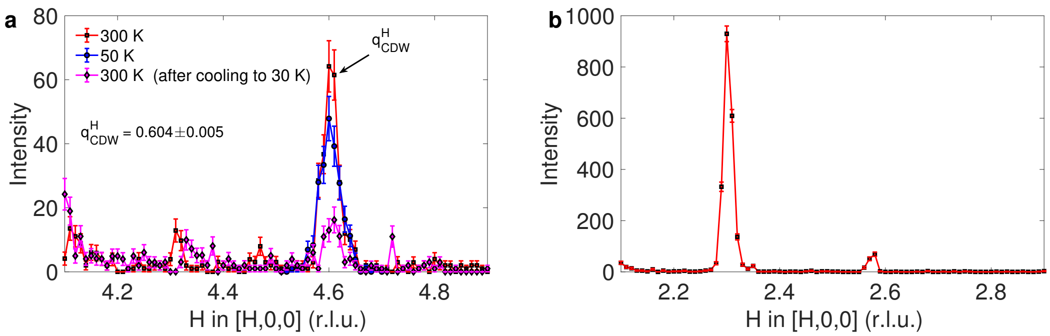

FIG. 5. (a) EXS mapping of CDW state along $[H, 0, 0]$ $(4 < H < 5)$ at 300 K, on cooling to 50 K, and after re-heating back to 300 K (thermal cycling 300 K $\rightarrow$ 30 K $\rightarrow$ 50 K $\rightarrow$ 300 K), showing CDW peak corresponding to $\mathbf{q}^H_{\mathrm{CDW}} = 0.604(5)$ r.l.u. Intensity represents the number of EXS photon counts per 5 seconds. Errors bars are from counting statistics ($\sqrt{N}$). (b) Observation of additional peaks along $[H, 0, 0]$ $(2 < H < 3)$ at $H = 2.30$ and 2.57 r.l.u.

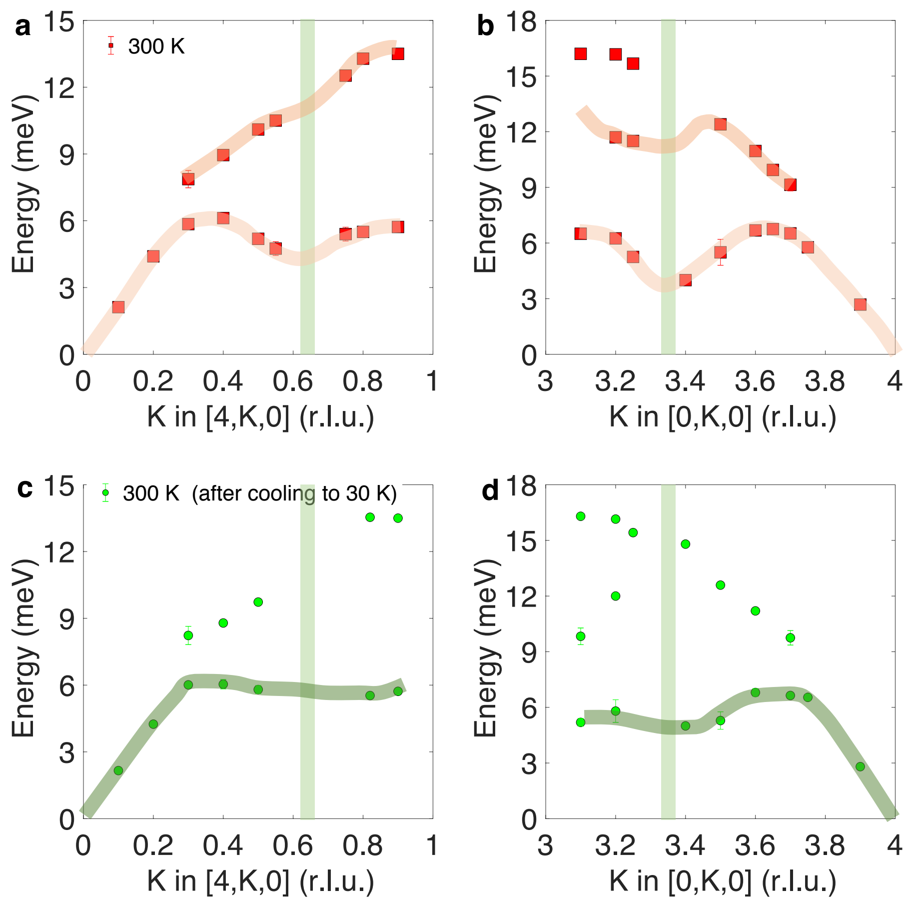

FIG. 6. (a) Phonon dispersion along $[4, K, 0]$ (a-polarized excitations propagating along K) at 300 K showing amplitude mode (near ∼4.5 meV) and Kohn anomaly (in optic branch) at $\mathbf{q}^K_{\mathrm{CDW1}}$ (light green vertical strip). Error bars, wherever visible, are one standard deviation on either side of the marker from the fitting of the damped harmonic oscillator (see SM section B1). (b) Same as panel (a) but along $[0, K, 0]$ (b-polarized excitations propagating along K), showing Kohn anomalies at 4-$\mathbf{q}^K_{\mathrm{CDW1}} = 3.357$ r.l.u. (c,d) Same as panels (a) and (b) but after the thermal cycling 300 K → 30 K → 300 K to access the other metastable state. Light red and green color lines above the markers are guides to the eye following the lattice dynamical susceptibility simulations (see SM section C3). Data points at $\mathbf{q}^K_{\mathrm{CDW1}}$ or in close vicinity are not shown as strong CDW peak intensity saturates the entire energy scan, and phonon intensity is not visible.

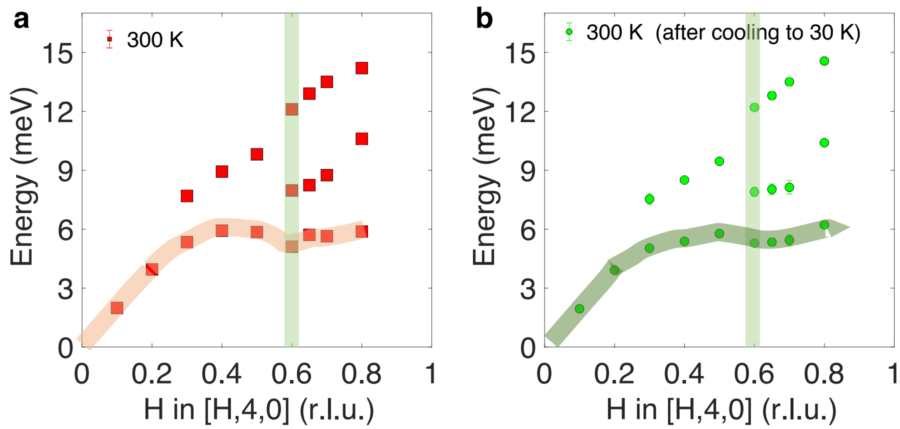

FIG. 7. (a) Phonon dispersion along $[H, 4, 0]$ (b-polarized excitations propagating along H) at 300 K showing Kohn anomaly at $\mathbf{q}^H_{\mathrm{CDW}}$ (light green vertical strip). Error bars, wherever visible, are one standard deviation on either side of the marker from the fitting of the damped harmonic oscillator (see Supplementary Materials). (b) Same as panel (a) but after the thermal cycling $300\,\mathrm{K} \rightarrow 30\,\mathrm{K} \rightarrow 300\,\mathrm{K}$ to access the other metastable state.

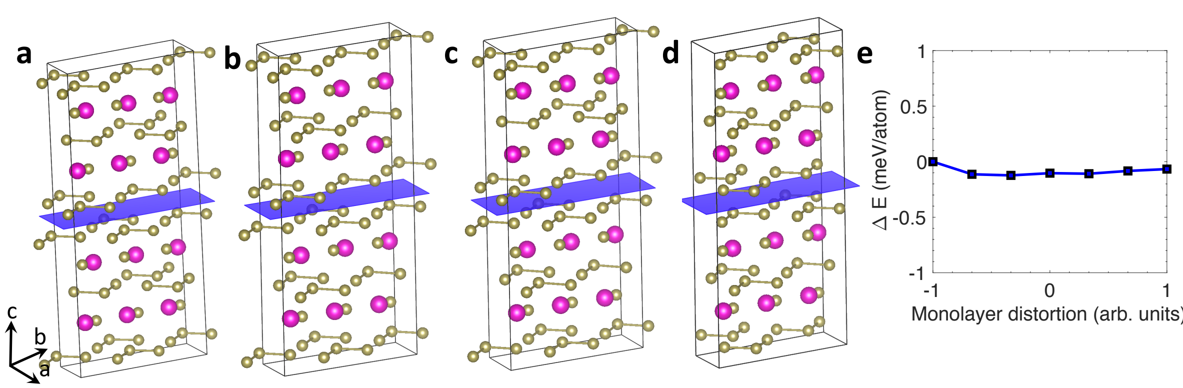

FIG. 8. (a-d) Different configurations of $EuTe_4$ structure with in- and out-of-phase displacements of mono- and bilayer along with doubling of the unit cell along the c-axis. The blue plane separates the two adjacent unit cells. (e) Change in energy in the NEB simulations between the configuration shown in panel (a) (corresponding to -1 on the x-axis), gradually decreasing the monolayer distortion to zero (corresponding to 0 on the x-axis), and then increasing the monolayer distortion to another side (corresponding to 1 on the x-axis).